Materials Research Bulletin 101 (2018) 199–204

Contents lists available at ScienceDirect

Materials Research Bulletin

journal homepage: www.elsevier.com/locate/matresbu

Enhancement of three-photon near-infrared quantum cutting in β-$NaYF_4$:Er^{3+} nanoparticles by Ag nanocubes

Biao Zheng[a,b], Lin Lin[a,b,c,*], Lili Huang[a,b], Zhuohong Feng[a,b,c], Luoqing Zhuang[a,b], Zhezhe Wang[a,b,c], Zhiqiang Zheng[a,b,c,*]

[a] College of Physics and Energy, Fujian Normal University, Fuzhou 350117, China
[b] Fujian Provincial Key Laboratory of Quantum Manipulation and New Energy Materials, Fujian Normal University, Fuzhou 350117, China
[c] Fujian Provincial Collaborative Innovation Center for Optoelectronic Semiconductors and Efficient Devices, Xiamen 361005, China

ARTICLE INFO

Keywords:
A. optical materials
A. nanostructure
B. luminescence
C. infrared spectroscopy
D. phosphors

ABSTRACT

The near-infrared (NIR) quantum cutting (QC) nanoparticles (NPs) β-$NaYF_4$:Er^{3+} are prepared by coprecipitation method. Three-photon NIR QC luminescence at 1520 nm ($^4I_{13/2} \rightarrow {}^4I_{15/2}$) is obtained under the excitation of 519 nm ($^4I_{15/2} \rightarrow {}^2H_{11/2}$). The corresponding QC efficiency η_{QC} calculated from the luminescence decay curves reaches as 242.59%. Furthermore, three-photon NIR QC luminescence is enhanced by the localized surface plasmon resonance of Ag nanocubes (NCs). The influence of Ag NCs concentration on three-photon QC luminescence is investigated, and the results show that the optimal concentration of Ag NCs is 0.10% with the enhancement factor reached a maximum as 2.86. Our study may have potential application as a QC layer to improve the photovoltaic conversion efficiency of germanium (Ge) solar cells.

1. Introduction

The increasing demand for solar energy, due to the gradual exhaustion of traditional fossil energy sources and the pollution of the environment, has put how to improve the photovoltaic conversion efficiency of solar cells at the forefront of research [1,2]. Low photovoltaic conversion efficiency mainly arises from the mismatch between the solar spectrum and the band gap energy of solar cells [3,4]. That is, photons with energy lower than the band gap cannot be absorbed, while for photons with energy larger than the band gap, the excess energy is lost by thermalization of hot charge carriers [5]. To make full use of solar energy, many scientists have put efforts on solar spectrum modulation through quantum cutting (QC) [6–14]. The QC process can convert one high-energy photon into two or more low-energy photons, which can be efficiently absorbed by solar cells [15,16]. Therefore, solar spectrum modulation by means of QC process is a significant and meaningful pathway to improve conversion efficiency of solar cells.

Recently, noble metal nanoparticles (NPs), such as silver and gold, have been used to enhance upconversion luminescence of rare-earth (RE) ions via the localized surface plasmon resonance (LSPR) [17–22]. This enhancement mechanism is that noble metal NPs can boost excitation efficiency or the radiative transition rate of RE ions when the LSPR wavelength of noble metal NPs matches with the excitation or emission wavelength of RE ions [21]. However, few papers have been reported about plasmon-enhanced QC luminescence by noble metal NPs. Despite our group have first reported the plasmon-enhanced QC luminescence in Tb^{3+}-Yb^{3+} co-doped phosphor by Ag NPs [13], it is still an inefficient enhanced QC luminescence. On one hand, the LSPR of Ag NPs at 420 nm does not match well with the excitation wavelength of Tb^{3+} ions at 374 nm. On the other hand, the energy transfer (ET) mechanism from Tb^{3+} ions to Yb^{3+} ions is second-order cooperative ET. The probability of second-order cooperative ET is 10^3 times lower than the probability of first-order resonant ET [7]. Additionally, it would be more preferred and efficient for solar spectrum modulation if one high-energy photon can be converted into three or more low-energy photons through QC process. To overcome these shortcomings, another noble metal NPs, whose LSPR has large overlap with the excitation wavelength of RE ions, is desired. Furthermore, RE ions, with first-order resonant ET mechanism and three or more photons QC luminescence property, are also preferred.

In this paper, single-doped β-$NaYF_4$:Er^{3+} NPs are synthesized, and three-photon near-infrared (NIR) QC luminescence at 1520 nm ($^4I_{13/2} \rightarrow {}^4I_{15/2}$) of Er^{3+} ion is obtained through two-step cross-relaxation ET under the excitation of 519 nm ($^4I_{15/2} \rightarrow {}^2H_{11/2}$). The corresponding QC efficiency η_{QC} is calculated from the luminescence decay curves. Furthermore, Ag nanocubes (NCs), whose LSPR match well with the excitation wavelength of Er^{3+} ion, are prepared. Then, β-$NaYF_4$:Er^{3+} NPs are decorated with Ag NCs. Plasmon-enhanced three-photon NIR

* Corresponding authors at: College of Physics and Energy, Fujian Normal University, Fuzhou 350117, China.
E-mail addresses: llin@fjnu.edu.cn (L. Lin), zqzheng@fjnu.edu.cn (Z. Zheng).

https://doi.org/10.1016/j.materresbull.2018.01.027
Received 23 September 2017; Received in revised form 18 January 2018; Accepted 19 January 2018

QC luminescence is realized by Ag NCs, and the corresponding NIR QC luminescence enhancement mechanism, boosting the excitation efficiency of Er^{3+} ion, is demonstrated through finite-difference time-domain (FDTD) method. Additionally, the influence of Ag NCs concentration on three-photon QC luminescence is also investigated. It is worthy to note that three-photon NIR QC luminescence of Er^{3+} ion in the QC host of β-$NaYF_4$ NPs and plasmon-enhanced three-photon NIR QC luminescence have not been reported before. Thanks to the energy bandgap of germanium (Ge) is about 0.67 eV (~1850–2000 nm), a little smaller than the three-photon NIR QC luminescence in β-$NaYF_4$:Er^{3+} NPs (~1520 nm), our study may have potential application for Ge solar cells to improve the photovoltaic conversion efficiency.

2. Experimental section

The β-$NaYF_4$ NPs were chosen as QC host owing to its high thermal and chemical stability and low phonon frequencies [19]. 2 mmol β-$NaYF_4$:Er^{3+} NPs were prepared through coprecipitation method following the protocols reported previously [5]. The Ag NCs solutions (1 ml containing 1.5625×10^{-5} mol Ag NCs) were synthesized by chemical reduction method [23]. In brief, Ag^+ was reduced to Ag by 1,5-pentanediol in the presence of poly (vinylpyrrolidone) (PVP) and a trace amount of cupric chloride ($CuCl_2$), in which PVP will selectively attach to {100} Ag facets and facilitate further the formation of a cubic shape [24]. Finally, β-$NaYF_4$:Er^{3+} NPs were decorated with Ag NCs homogeneously by a facile method: Firstly, a proper amount of as-synthesized β-$NaYF_4$:Er^{3+} NPs and Ag NCs solution were added into a centrifuge tube and ultrasonic oscillated for 1 h to create an uniform mixture. Then the mixture were transferred into a agate mortar and dried out at 60 °C for 8 h. Thanks to the Ag NCs are coated with a thin PVP layer during its synthesis process, which possesses excellent adsorption ability and will adsorb β-$NaYF_4$:Er^{3+} NPs to the surface of Ag NCs [25]. Furthermore, the process of drying the mixture to powder will make the structure of β-$NaYF_4$:Er^{3+} NPs decorated with Ag NCs more stable. In this manner, β-$NaYF_4$:Er^{3+} NPs decorated Ag NCs were generated, the corresponding synthesis schematic illustration is shown in Fig. 1. To investigate the influence of Ag NCs concentration on three-photon NIR QC luminescence, a series of β-$NaYF_4$:Er^{3+} NPs decorated with x% Ag NCs (x = 0, 0.05, 0.10, 0.15, 0.20) were prepared. Here, Er/Ag was calculated by mole ratio. The amount of β-$NaYF_4$:4%Er^{3+} NPs was 2 mmol (0.3821 g). The corresponding volume of Ag NCs solutions were 64 µl (0.05% Ag), 128 µl (0.10% Ag), 192 µl (0.15% Ag), and 256 µl (0.20% Ag), respectively.

As-prepared samples were characterized by X-ray diffraction (XRD, MiniFlexII, Rigaku), scanning electron microscope (SEM, SU8010, Hitachi), absorption spectra (Lambda 950, PerkinElmer), and fluorescence spectra (Fluorolog 3-22 spectrofluorometer, Horiba Jobin Yvon). Specifically, the fluorescence spectra in the same figure were measured by the same spectrofluorometer in one experiment under the same measuring conditions. Therefore, the intensity of these spectra in one figure is comparable.

3. Results and discussion

3.1. Three-photon NIR QC luminescence of β-$NaYF_4$:Er^{3+} NPs

The crystal structure of the β-$NaYF_4$:Er^{3+} NPs is identified by XRD. As shown in Fig. 2(a), all major diffraction peaks match well with the standard powder diffraction file card No. 16-0334 and no other impurity peak is detected, indicating that pure β-$NaYF_4$:Er^{3+} NPs have been synthesized and doped Er^{3+} ions can substitute Y^{3+} ions without disturbing the crystal lattice. The SEM image of β-$NaYF_4$:Er^{3+} NPs is shown in Fig. 2(b), indicating that the β-$NaYF_4$:Er^{3+} NPs are well-dispersed and have an average diameter of 20 nm.

The NIR emission spectra of β-$NaYF_4$ NPs doped with different Er^{3+} ion concentrations under the excitation of 519 nm are depicted in Fig. 3(a). The major emission peak located at 1520 nm is attributed to the $^4I_{13/2} \rightarrow {}^4I_{15/2}$ transition of Er^{3+} ions. According to the relationship between NIR emission intensity at 1520 nm and different Er^{3+} ion concentration in the inset of Fig. 3(a), NIR emission intensity firstly increases with increasing Er^{3+} concentration, and reaches the maximum while the Er^{3+} concentration is 4%, then decreases due to the concentration quenching. Therefore, the optimal Er^{3+}-doped concentration is considered as 4%. Fig. 3(b) shows the Vis – NIR emission spectrum of β-$NaYF_4$:4%Er^{3+} NPs under the excitation of 519 nm. The major emission peaks are assigned to $^4S_{3/2} \rightarrow {}^4I_{15/2}$ (541 nm), $^4F_{9/2} \rightarrow {}^4I_{15/2}$ (654 nm), $^4I_{9/2} \rightarrow {}^4I_{15/2}$ (808 nm), $^4I_{11/2} \rightarrow {}^4I_{15/2}$ (980 nm), $^2H_{11/2} \rightarrow {}^4I_{9/2}$ (1211 nm), and $^4I_{13/2} \rightarrow {}^4I_{15/2}$ (1520 nm) transitions of Er^{3+} ions [10,11]. The corresponding fluorescence intensity proportions are calculated in the inset of Fig. 3(b). It is clear that most of the fluorescence energy (~96.22%) is concentrated on the transition of $^4I_{13/2} \rightarrow {}^4I_{15/2}$ (1520 nm) under the excitation of 519 nm.

To confirm the NIR emission at 1520 nm under the excitation of 519 nm is a three-photon NIR QC luminescence process, the excitation spectra of β-$NaYF_4$ NPs doped with different Er^{3+} ion concentrations monitored at 541 nm and 1520 nm are measured in Fig. 4(a) and Fig. 4(b), respectively. We found that the excitation spectra monitored at 541 nm and 1520 nm are very similar in shape of the waveform and in the peak wavelengths. The major excitation peaks are assigned to $^4I_{15/2} \rightarrow {}^4G_{9/2}$ (363 nm), $^4I_{15/2} \rightarrow {}^4G_{11/2}$ (377 nm), $^4I_{15/2} \rightarrow {}^2H_{9/2}$ (404 nm), $^4I_{15/2} \rightarrow {}^4F_{5/2}$ (448 nm), $^4I_{15/2} \rightarrow {}^4F_{7/2}$ (488 nm), and $^4I_{15/2} \rightarrow {}^2H_{11/2}$ (519 nm) transitions of Er^{3+} ions [10,11]. When the concentration of Er^{3+} ions increases from 1% to 4%, the visible excitation and fluorescence intensities decrease, with a concomitant enhancement

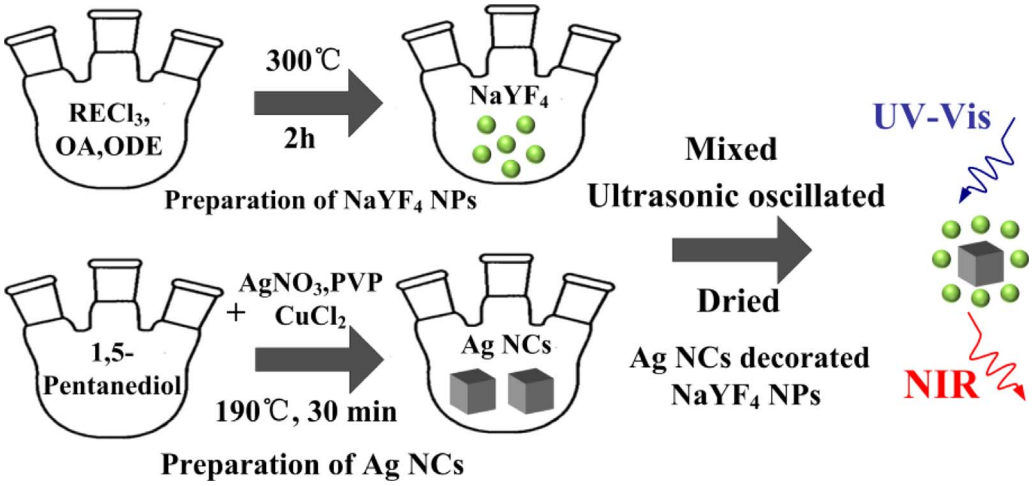

Fig. 1. Schematic illustration of the synthesis of β-$NaYF_4$:Er^{3+} NPs decorated with Ag NCs.

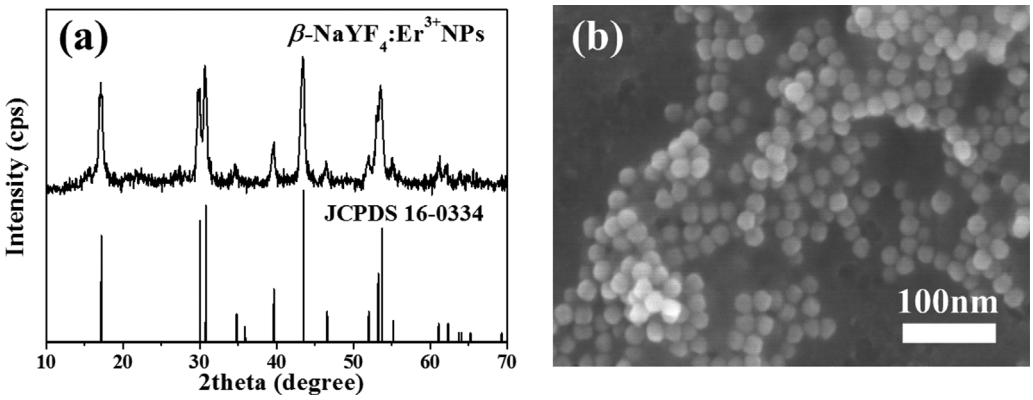

Fig. 2. (a) XRD patterns of β-$NaYF_4$:Er^{3+} NPs. (b) SEM image of β-$NaYF_4$:Er^{3+} NPs.

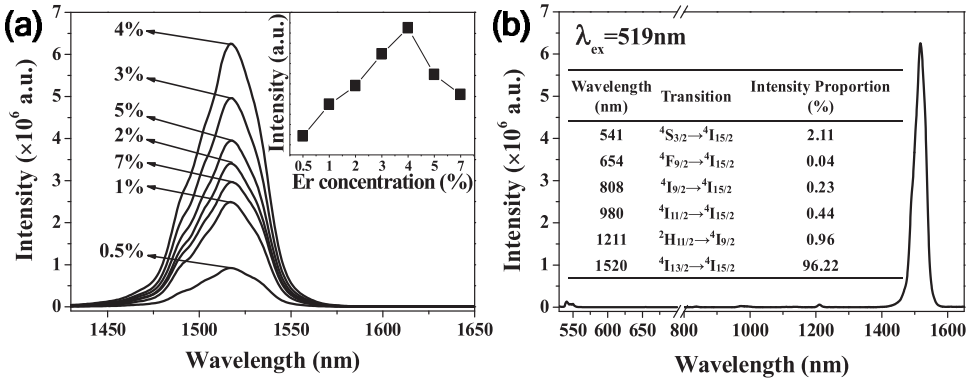

Wavelength (nm)	Transition	Intensity Proportion (%)
541	$^4S_{3/2}\rightarrow{}^4I_{15/2}$	2.11
654	$^4F_{9/2}\rightarrow{}^4I_{15/2}$	0.04
808	$^4I_{9/2}\rightarrow{}^4I_{15/2}$	0.23
980	$^4I_{11/2}\rightarrow{}^4I_{15/2}$	0.44
1211	$^2H_{11/2}\rightarrow{}^4I_{9/2}$	0.96
1520	$^4I_{13/2}\rightarrow{}^4I_{15/2}$	96.22

Fig. 3. (a) NIR emission spectra of β-$NaYF_4$: x%Er^{3+} NPs under the excitation of 519 nm (x = 0.5, 1, 2, 3, 4, 5, 7). Inset: NIR emission intensity at 1520 nm vs. Er^{3+} concentration. (b) Vis – NIR emission spectrum (λ_{ex} = 519 nm) of β-$NaYF_4$:4%Er^{3+} NPs. Inset: Intensity proportions of measured fluorescence transitions.

in the NIR excitation and fluorescence intensities. These results indicate that NIR emission at 1520 nm may ascribe to two-step cross-relaxation ET from $^4S_{3/2}$ level to $^4I_{13/2}$ level (CR1:$^4S_{3/2}$ + $^4I_{15/2}\rightarrow{}^4I_{9/2}$ + $^4I_{13/2}$, CR2: $^4I_{9/2}$ + $^4I_{15/2}\rightarrow{}^4I_{13/2}$ + $^4I_{13/2}$) under the excitation of 519 nm [6].

To further certify that NIR emission at 1520 nm is caused by two-step cross-relaxation ET (CR1, CR2), the decay curves of Er^{3+} $^4S_{3/2}$ level and $^4I_{9/2}$ level in β-$NaYF_4$:x%Er^{3+} NPs under the excitation of 519 nm are measured in Fig. 5(a) and Fig. 5(b), respectively. It can be observed that $^4S_{3/2}$ level and $^4I_{9/2}$ level decays faster and faster with the increase of Er^{3+} concentration, which confirms the existence of two-step cross-relaxation ET. These results indicate that the NIR emission at 1520 nm under the excitation of 519 nm is a three-photon NIR QC luminescence process. In addition, the lifetimes τ of $^4S_{3/2}$ level and $^4I_{9/2}$ level doped with different Er^{3+} concentrations are calculated from the decay curves by using Eq. (1) [4,15]:

$$\tau = \int I(t)/I_0 dt \tag{1}$$

Where $I(t)$ is the luminescence intensity as a function of decay time t, and I_0 is the maximum of $I(t)$ at the initial time (t = 0). The calculated lifetime values are listed in Table 1. The lifetime values τ descend while Er^{3+} concentration increases, further confirming the analysis above.

According to the majority of the literature in the field of QC luminescence, ET efficiency and QC luminescence efficiency are two main parameters. In our work, the cross-relaxation ET efficiency η_{CR} of $^4S_{3/2}$ level and $^4I_{9/2}$ level doped with different Er^{3+} concentrations can be calculated using Eq. (2) [4,15]:

$$\eta_{CR} = 1 - \frac{\tau(x\%Er)}{\tau(0.1\%Er)} \tag{2}$$

Where τ denotes the lifetime and x%Er represents the concentration of Er^{3+} ions. It is assumed that cross-relaxation ET between Er^{3+} ions is small and can be ignored when x = 0.1% [11]. Therefore, τ (0.1%Er) can be regarded as the case of no cross-relaxation ET. The calculated cross-relaxation ET efficiency values are listed in Table 1.

To calculate the theoretical up-limit three-photon QC luminescence efficiency η_{QC} at 1520 nm under the excitation of 519 nm, we assume the luminescence efficiencies of the Er^{3+} ion energy levels (e.g., $^4S_{3/2}$,

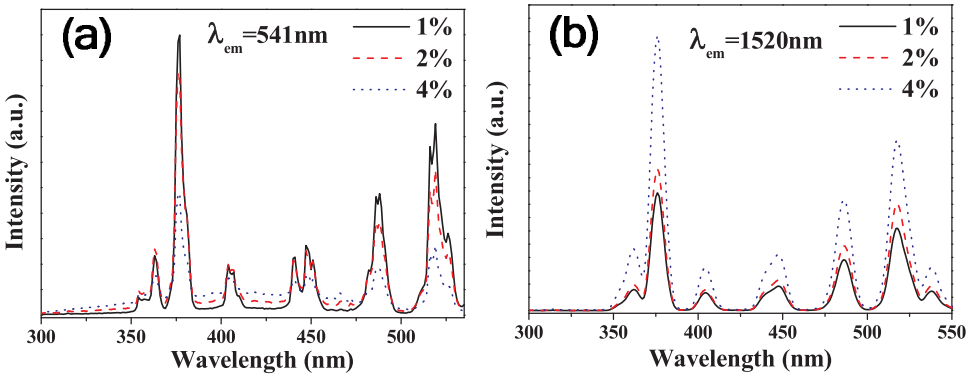

Fig. 4. Excitation spectra monitored at (a) 541 nm and (b) 1520 nm of β-$NaYF_4$: x%Er^{3+} NPs (x = 1, 2, 4).

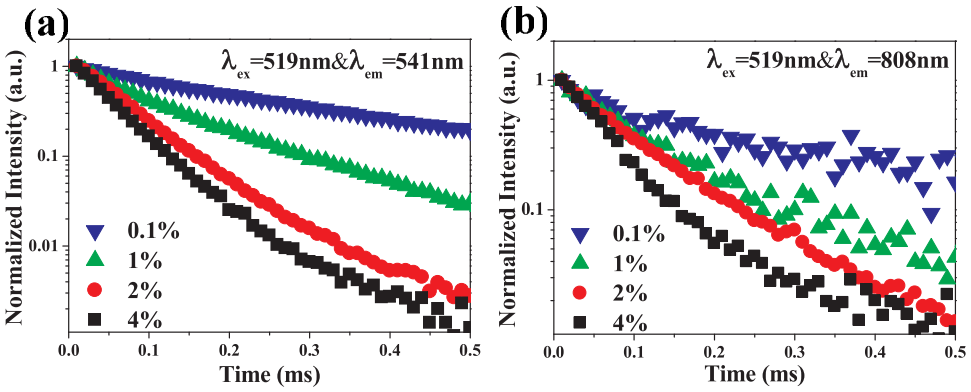

Fig. 5. Luminescence decay curves of Er^{3+} (a) $^4S_{3/2}$ level and (b) $^4I_{9/2}$ level in β-$NaYF_4$: x%Er^{3+} NPs (x = 0.1, 1, 2, 4).

Table 1
Three-photon QC luminescence parameters of β-$NaYF_4$ NPs doped with different Er^{3+} ion concentrations.

Er^{3+} concentration (%)	τ ($^4S_{3/2}$) (ms)	τ ($^4I_{9/2}$) (ms)	η_{CR1} (%)	η_{CR2} (%)	η_{QC} (%)
0.1	0.29532	0.20934	–	–	–
1	0.11322	0.10264	61.66	50.97	193.09
2	0.06451	0.09135	78.16	56.36	222.21
4	0.04968	0.05983	83.18	71.42	242.59

$^4I_{9/2}$, and $^4I_{13/2}$) as 1, as is assumed in most of the research literature on QC luminescence [4,11,15]. Therefore, the theoretical QC luminescence efficiency η_{QC} can be expressed as Eq. (3) [11]:

$$\eta_{QC} = 1 + \eta_{CR}(^4S_{3/2}) + \eta_{CR}(^4S_{3/2})\eta_{CR}(^4I_{9/2}) \quad (3)$$

The calculated QC luminescence efficiency values are listed in Table 1. It can be observed that η_{QC} reaches 242.59% at the optimal Er^{3+}-doped concentration of 4%. To our knowledge, the η_{QC} of 242.59% is higher than any other reported three-photon NIR QC luminescence of Er^{3+} ion [6,10,11].

In order to illustrate the three-photon NIR QC luminescence process, the schematic diagram of the energy levels of Er^{3+} ion is plotted as Fig. 6. Firstly, when Er^{3+} ion is excited from ground state $^4I_{15/2}$ to excited state $^2H_{11/2}$ under the excitation of 519 nm, two dominant processes containing multi-phonon nonradiative relaxation ($^2H_{11/2} \rightarrow {}^4S_{3/2}$) and radiative transition ($^2H_{11/2} \rightarrow {}^4I_{9/2}$) occur. Subsequently, Er^{3+} ion on state $^4S_{3/2}$ undergo three main processes: radiative transition ($^4S_{3/2} \rightarrow {}^4I_{15/2}$), multi-phonon nonradiative relaxation ($^4S_{3/2} \rightarrow {}^4F_{9/2}$) leading to the radiative transition ($^4F_{9/2} \rightarrow {}^4I_{15/2}$), and cross-relaxation (CR1:$^4S_{3/2} + {}^4I_{15/2} \rightarrow {}^4I_{9/2} + {}^4I_{13/2}$). Similarly, Er^{3+} ions on state $^4I_{9/2}$ also experience the radiative transition ($^4I_{9/2} \rightarrow {}^4I_{15/2}$), multi-phonon relaxation ($^4I_{9/2} \rightarrow {}^4I_{11/2}$) and cross-relaxation (CR2: $^4I_{9/2} + {}^4I_{15/2} \rightarrow {}^4I_{13/2} + {}^4I_{13/2}$) processes. Finally, three Er^{3+} ions on the state $^4I_{13/2}$ radiate to the ground state $^4I_{15/2}$ and emit three photons at 1520 nm simultaneously. In this way, three-photon NIR QC luminescence at 1520 nm is achieved through two-step cross-relaxation ET under the excitation of 519 nm.

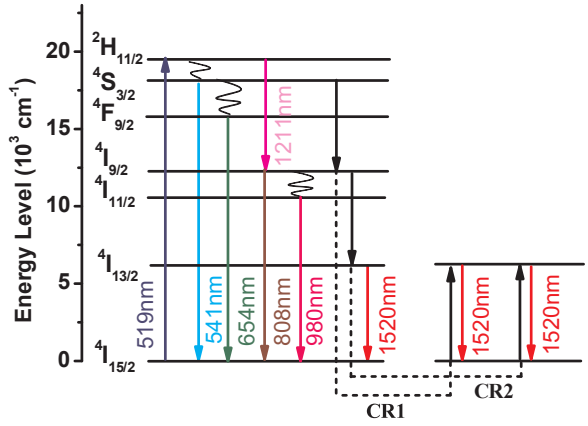

Fig. 6. Schematic diagram of the energy levels of Er^{3+} ion in three-photon NIR QC luminescence.

3.2. Plasmon-enhanced three-photon NIR QC luminescence of β-$NaYF_4$:Er^{3+} NPs by Ag NCs

As we mentioned in the Introduction section, three-photon NIR QC luminescence of β-$NaYF_4$:Er^{3+} NPs can be enhanced by the LSPR of Ag NCs. Therefore, Ag NCs are synthesized to enhance the three-photon NIR QC luminescence of Er^{3+} ions. The morphology and size of Ag NCs is examined by SEM, as shown in Fig. 7(a). It can be seen that the Ag NCs are uniform and well-dispersed, with an average edge length of 90 nm. The corresponding UV − vis absorption spectrum of Ag NCs solution is measured in Fig. 7(b). Four plasmon resonance peaks are observed. The strong broad absorption band centered at 515 nm is originated from dipolar plasmon mode, while the weak absorption peaks located at 354 nm, 386 nm, and 445 nm may be ascribed to octupolar, quadrupolar and quadrupolar plasmon modes, respectively [26]. Due to the dipolar plasmon mode of Ag NCs at 515 nm matches well with the excitation wavelength of Er^{3+} ions at 519 nm, Ag NCs can be applied to decorate the β-$NaYF_4$:Er^{3+} NPs to enhance the three-photon NIR QC luminescence via boosting the excitation efficiency.

To observe the distribution of Ag NCs in β-$NaYF_4$:Er^{3+} NPs, the SEM image of β-$NaYF_4$:Er^{3+} NPs decorated with Ag NCs is measured in Fig. 8. It is obvious that Ag NCs are surrounded by β-$NaYF_4$:Er^{3+} NPs homogeneously. Moreover, the cluster of Ag NCs or β-$NaYF_4$:Er^{3+} NPs does not occur. It is well known that the local electric field generated by Ag NCs has an effective enhancement range, which is about 30 nm from the Ag NCs surface [27]. Therefore, only the excitation efficiency of β-$NaYF_4$:Er^{3+} NPs, which lies in effective enhancement range, can be enhanced by Ag NCs. The other β-$NaYF_4$:Er^{3+} NPs, which lies out of the effective enhancement range, are not enhanced. Consequently, in our experiment, the enhancement of three-photon NIR QC luminescence of β-$NaYF_4$:Er^{3+} NPs by Ag NCs is considered as an average enhancement effect.

To realize plasmon-enhanced three-photon NIR QC luminescenc, the NIR emission spectra of β-$NaYF_4$:Er^{3+} NPs decorated with different Ag NCs concentrations are measured in Fig. 9(a). The NIR QC luminescence intensity at 1520 nm increases with increasing Ag NCs concentration until it reaches 0.10%, then decreases. The maximum NIR QC luminescence enhances about 2.86 fold when the Ag NCs concentration is 0.10%. The NIR QC luminescence enhancement mechanism can be explained as follows: Since the excitation peak of Er^{3+} ion at 519 nm matches well with the LSPR of Ag NCs at 515 nm, the excitation efficiency of Er^{3+} ion will be enhanced, leading to rise of the excited state population of Er^{3+} ion, which will enhance the NIR

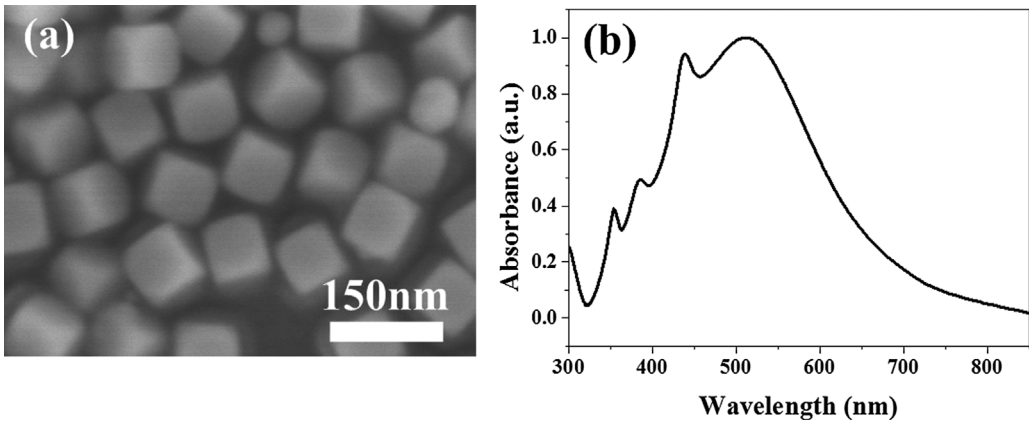

Fig. 7. (a) SEM image of Ag NCs. (b) UV − vis absorption spectrum of Ag NCs.

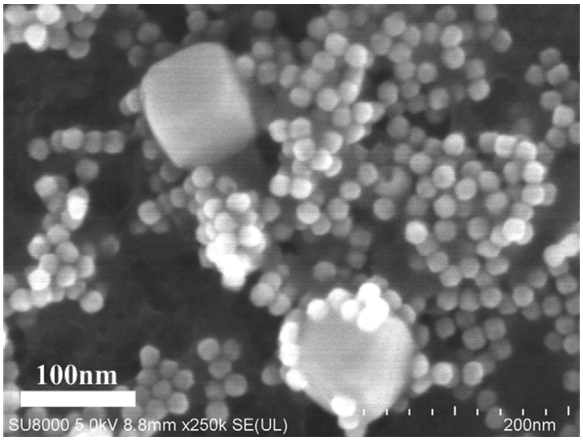

Fig. 8. SEM image of β-$NaYF_4$:Er^{3+} NPs decorated with Ag NCs.

emission at 1520 nm via two-step cross-relaxation ET. In this way, plasmon-enhanced three-photon NIR QC luminescence is achieved. Additionally, it should be noted that the QC luminescence intensity begins to decrease when the Ag NCs concentration exceeds 0.10%. This phenomenon may mainly cause by the stronger extinction on the incident light due to the larger concentration of Ag NCs [28].

To further demonstrate that three-photon NIR QC luminescence enhancement is ascribed to the LSPR of Ag NCs, the electric field intensities and distributions around single Ag NC are simulated by the FDTD solution software. The incidence light of 519 nm is launched into a box containing an Ag NC, as shown in Fig. 9(b). It is clearly seen that the electric field intensities around Ag NC are enhanced, which will enhance three-photon NIR QC luminescence through effective coupling between the LSPR of Ag NCs and excitation efficiency of Er^{3+} ion [22].

4. Conclusions

In this work, β-$NaYF_4$:Er^{3+} NPs and Ag NCs are synthesized by the coprecipitation method and chemical reduction method, respectively. Three-photon NIR QC luminescence of β-$NaYF_4$:Er^{3+} NPs at 1520 nm is obtained through two-step cross-relaxation ET under the excitation of 519 nm. The corresponding QC efficiency η_{QC} calculated from luminescence decay curves reaches a maximum as high as 242.59% at the optimal Er^{3+}-doped concentration of 4%. Furthermore, plasmon-enhanced three-photon NIR QC luminescence is realized in β-$NaYF_4$:Er^{3+} NPs decorated with Ag NCs, and the corresponding enhancement mechanism, boosting the excitation efficiency of Er^{3+} ion, is demonstrated through FDTD method. The influence of Ag NCs concentration on three-photon NIR QC luminescence is also investigated. The maximum QC luminescence enhancement factor is about 2.86 when the concentration of Ag NCs is 0.10%. Our study may provide a promising QC layer on the top of Ge solar cells to improve the photovoltaic conversion efficiency.

Acknowledgements

This work was supported by National Natural Science Foundation of China (No. 11204039 and No. 51202033); Natural Science Foundation of Fujian Province of China (No. 2015J01243, No. 2016J01213 and No.

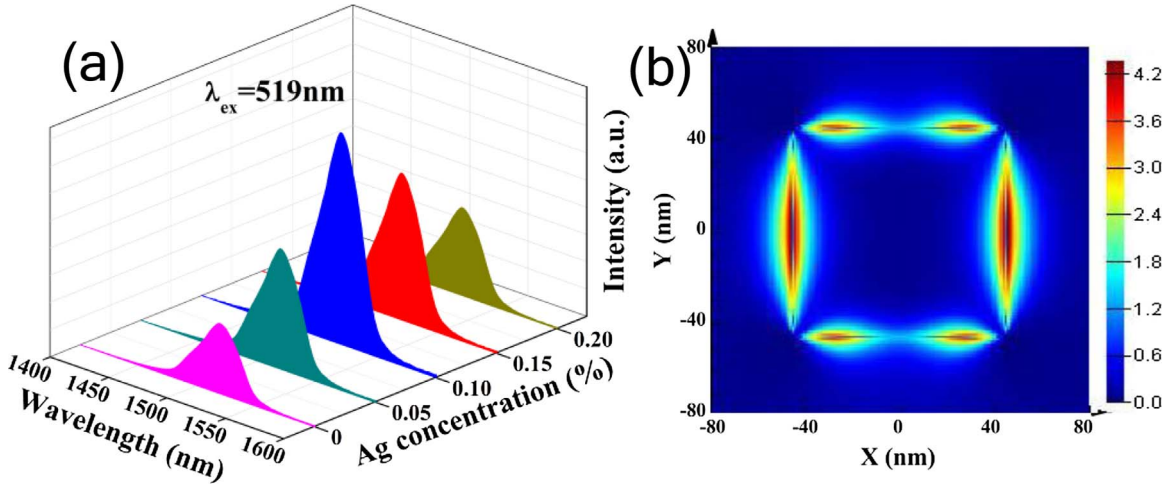

Fig. 9. (a) NIR emission spectra (λ_{ex} = 519 nm) of β-$NaYF_4$:Er^{3+} NPs decorated with x% Ag NCs (x = 0, 0.05, 0.10, 0.15, 0.20). (b) Contour of simulated electric field distribution around Ag NCs excited at 519 nm.

2017J01399).

References

[1] C. Strümpel, M. McCann, G. Beaucarne, V. Arkhipov, A. Slaoui, V. Švrček, C. del Cañizo, I. Tobias, Modifying the solar spectrum to enhance silicon solar cell efficiency—an overview of available materials, Sol. Energy Mater. Sol. Cells 91 (2007) 238–249.

[2] B.M. van der Ende, L. Aarts, A. Meijerink, Near-infrared quantum cutting for photovoltaics, Adv. Mater. 21 (2009) 3073–3077.

[3] B.S. Richards, Luminescent layers for enhanced silicon solar cell performance: down-conversion, Sol. Energy Mater. Sol. Cells 90 (2006) 1189–1207.

[4] P. Vergeer, T. Vlugt, M. Kox, M. den Hertog, J. van der Eerden, A. Meijerink, Quantum cutting by cooperative energy transfer in $Yb_xY_{1-x}PO_4:Tb^{3+}$, Phys. Rev. B 71 (2005) 014119.

[5] W. Zhu, D. Chen, L. Lei, J. Xu, Y. Wang, An active-core/active-shell structure with enhanced quantum-cutting luminescence in Pr–Yb co-doped monodisperse nanoparticles, Nanoscale 6 (2014) 10500–10504.

[6] X. Chen, J. Wu, X. Xu, Y. Zhang, N. Sawanobori, C. Zhang, Q. Pan, G.J. Salamo, Three-photon infrared quantum cutting from single species of rare-earth Er^{3+} ions in $Er0.Gd_{0.7}VO_4$ crystalline, Opt. Lett. 34 (2009) 887–889.

[7] D.C. Yu, X.Y. Huang, S. Ye, Q.Y. Zhang, Efficient first-order resonant near-infrared quantum cutting in β-$NaYF_4:Ho^{3+},Yb^{3+}$, J. Alloy Compd. 509 (2011) 9919–9923.

[8] H. Lin, D. Chen, Y. Yu, A. Yang, Y. Wang, Near-infrared quantum cutting in Ho^{3+}/Yb^{3+} codoped nanostructured glass ceramic, Opt. Lett. 36 (2011) 876–878.

[9] K. Deng, T. Gong, L. Hu, X. Wei, Y. Chen, M. Yin, Efficient near-infrared quantum cutting in $NaYF_4:Ho^{3+},Yb^{3+}$ for solar photovoltaics, Opt. Express 19 (2011) 1749–1754.

[10] X. Huang, D. Chen, L. Lin, Z. Wang, Z. Feng, Z. Zheng, Infrared quantum cutting in Er^{3+}: $NaYF_4$ nanostructured glass ceramics for solar cells, Optik 125 (2014) 565–568.

[11] X. Chen, S. Li, K. Wang, Z. Wu, G. Zhao, J. Tao, H. Ma, W. Lin, H. Liu, L. Hu, P. Guo, G.J. Salamo, Two-photon, three-photon, and four-photon near-infrared quantum cutting luminescence of an Er^{3+} activator in tellurium glass phosphor, Appl. Opt. 55 (2016) 3343–3350.

[12] W. Xia, S. Xiao, X. Yang, X. Jin, Quantum cutting and tunable luminescence properties in $Pr^{3+}/Sm^{3+},Yb^{3+}$ co-doped $SrMoO_4$ powders, Mater. Res. Bull. 89 (2017) 5–10.

[13] B. Zheng, S. Xu, L. Lin, Z. Wang, Z. Feng, Z. Zheng, Plasmon enhanced near-infrared quantum cutting of KYF_4: Tb^{3+},Yb^{3+} doped with Ag nanoparticles, Opt. Lett. 40 (2015) 2630–2633.

[14] Q. Sun, S. Zhan, E. Liu, H. Miao, Y. Hao, G. Zhang, D. Zhang, J. Fan, X. Hu, The preparation and study of fluorescence properties of $Y_2O_3:Tb^{3+},Yb^{3+}$ doped with silver nanoparticles, Ceram. Int. 41 (2015) 12644–12650.

[15] S. Ye, B. Zhu, J. Chen, J. Luo, J.R. Qiu, Infrared quantum cutting in Tb^{3+},Yb^{3+} codoped transparent glass ceramics containing CaF_2 nanocrystals, Appl. Phys. Lett. 92 (2008) 141112.

[16] Q. Zhang, X. Huang, Recent progress in quantum cutting phosphors, Prog. Mater. Sci. 55 (2010) 353–427.

[17] W. Park, D. Lu, S. Ahn, Plasmon enhancement of luminescence upconversion, Chem. Soc. Rev. 44 (2015) 2940–2962.

[18] X. Chen, W. Xu, L. Zhang, X. Bai, S. Cui, D. Zhou, Z. Yin, H. Song, D.H. Kim, Large upconversion enhancement in the "Islands" Au–Ag alloy/$NaYF_4:Yb^{3+},Tm^{3+}/Er^{3+}$ composite films, and fingerprint identification, Adv. Funct. Mater. 25 (2015) 5462–5471.

[19] Y. Qin, Z. Dong, D. Zhou, Y. Yang, X. Xu, J. Qiu, Modification on populating paths of β-$NaYF_4$:Nd/Yb/Ho@SiO_2@Ag core/double-shell nanocomposites with plasmon enhanced upconversion emission, Opt. Mater. Express 6 (2016) 1942–1955.

[20] S. Fischer, D. Kumar, F. Hallermann, G. von Plessen, J.C. Goldschmidt, Enhanced upconversion quantum yield near spherical gold nanoparticles-a comprehensive simulation based analysis, Opt. Express 24 (2016) A460–A475.

[21] D.M. Wu, A. García-Etxarri, A. Salleo, J.A. Dionne, Plasmon-enhanced upconversion, J. Phys. Chem. Lett. 5 (2014) 4020–4031.

[22] B. Shao, Z. Yang, J. Li, J. Yang, Y. Wang, J. Qiu, Z. Song, Upconversion emission enhancement by porous silver films with ultra-broad plasmon absorption, Opt. Mater. Express 7 (2017) 1188–1197.

[23] C. Fang, Y.H. Lee, L. Shao, R. Jiang, J. Wang, Q.-H. Xu, Correlating the plasmonic and structural evolutions during the sulfidation of silver nanocubes, ACS Nano 7 (2013) 9354–9365.

[24] S.E. Skrabalak, L. Au, X. Li, Y. Xia, Facile synthesis of Ag nanocubes and Au nanocages, Nat. Protoc. 2 (2007) 2182–2190.

[25] S.F. Wei, J.S. Lian, Q. Jiang, Controlling growth of ZnO rods by polyvinylpyrrolidone (PVP) and their optical properties, Appl. Surf. Sci. 255 (2009) 6978–6984.

[26] Y.H. Lee, H. Chen, Q.-H. Xu, J. Wang, Refractive index sensitivities of noble metal nanocrystals: the effects of multipolar plasmon resonances and the metal type, J. Phys. Chem. C 115 (2011) 7997–8004.

[27] T. Ming, H. Chen, R. Jiang, Q. Li, J. Wang, Plasmon-controlled fluorescence: beyond the intensity enhancement, J. Phys. Chem. Lett. 3 (2012) 191–202.

[28] N.S. Abadeer, M.R. Brennan, W.L. Wilson, C.J. Murphy, Distance and plasmon wavelength dependent fluorescence of molecules bound to silica-coated gold nanorods, ACS Nano 8 (2014) 8392–8406.